Supplementary Information

Unraveling and suppressing the voltage decay of high-capacity cathode materials for sodium-ion batteries

Luoran Sun,‡ Zhonghan Wu,‡ Machuan Hou, Youxuan Ni, Haoxiang Sun, Peixin Jiao, Haixia Li, Wei Zhang, Liang Zhang, Kai Zhang,* Fangyi Cheng, Jun Chen

‡ These authors contributed equally to this work.

* Corresponding author: zhangkai_nk@nankai.edu.cn

Supplemental Experimental Procedures

Material preparations

$Na_{0.8}Li_{0.24}Al_xMn_{0.76-x}O_2$ (x = 0, 0.01, 0.03, 0.05) were synthesized *via* solid-state reactions. The stoichiometric mixtures of Na_2CO_3 (99.99%; Aladdin), $LiOH·H_2O$ (99.98%; Aladdin), Al_2O_3 (99.99%; Aladdin), and MnO_2 (99%; Aladdin) were ground and then calcined at 700 °C for 15 h. After cooling to room temperature, the products were transferred to an argon-filled glove box.

Electrochemical measurements

The electrochemical tests were carried out in CR2032 coin-type cells. The mixture of active material (80 wt.%), super P (10 wt.%) and polyvinylidene fluoride (PVdF) binder (10 wt.%) was dispersed in N-methyl pyrrolidone (NMP). The slurry was cast onto an Al foil and dried at 110 °C for 12 h under vacuum. The loading of the active material in the electrode was ~2 mg cm^{-2}. The coin cells were assembled in the argon-filled glove box using sodium foil as the anode, glass fiber filter paper as separator and 1.0 M $NaPF_6$ in PC containing 5 wt.% of FEC as the electrolyte. The galvanostatic charge-discharge tests were performed using a Neware battery test system (MIHW-200-160CH, Shenzhen, China) at 25 °C. Cyclic voltammetry was collected on CHI 660 electrochemistry station in a voltage range of 1.5–4.5 V with a scan rate of 0.2 mV s^{-1}. 1 C corresponds to 200 mA g^{-1} for all the electrochemical tests.

Characterization

The crystal structures of the samples were analyzed by powder X-ray diffraction (Rigaku, SmartLab 9KW, Cu K$_\alpha$ radiation), and Rietveld refinements were conducted with the GSAS and EXPGUI suite.[1] The morphologies and microstructures of the samples were characterized using a field emission scanning electron microscopy (FESEM, JEOL, JSM-7900F) and a transmission

electron microscopy (TEM, FEI, Talos F200X G2). The chemical composition of the samples was determined by an inductively coupled plasma-optical emission spectrometer (ICP-OES, Aglient 5110). ^{7}Li solid-state nuclear magnetic resonance (NMR, JNM-ECZ600R) experiments was performed using a 1 mm MAS probe at rotor spinning speed of 30 kHz. High-angle annular dark-field (HAADF) images and electron energy-loss spectroscopy (EELS) data were obtained using JEOL NEOARM 200F with a probe corrector at an acceleration voltage of 200 kV. The gas evolutions of different cathodes during the initial charge were detected by differential electrochemical mass spectrometry (DEMS) using a QAS 100 instrument (Linglu, Shanghai). Mn K-edge X-ray adsorption spectroscopy (XAS) of the samples were carried out at the beamline BL11B of the Shanghai Synchrotron Radiation Facility (SSRF) in Shanghai, China. The XAS data were collected in a transmission mode and processed through Demeter software package.[2] Oxygen K-edge soft XAS measurements were carried out in TFY (total fluorescence yield) mode at beamline 02B02 of the SSRF in Shanghai, China.

Computational details

Spin-polarized density functional theory calculations were carried out using Vienna ab initio simulation package (VASP).[3] The projector augmented wave (PAW) method with the Generalized Gradient Approximation (GGA) of Perdew-Burke-Ernzerhof (PBE) version was applied.[4, 5] The cut-off energy was chosen as 450 eV. The convergence criteria were set to 1×10^{-5} eV and 0.02 eV Å^{-1}, respectively. The Hubbard U potential correction was applied to take into account the self-interactions with the U value of 4.0 eV for Mn ions.[6] Based on the previous works,[7] the formation energy (ΔE_f) of NLAMO was obtained as follows:

$$\Delta E_f = E(Na_{18}Li_6AlMn_{11}O_{36}) - E(Na_{18}Li_6Mn_{12}O_{36}) - \frac{1}{2}E(Al_2O_3) + E(MnO_2) - \frac{1}{4}E(O_2)$$

Supplemental Figures
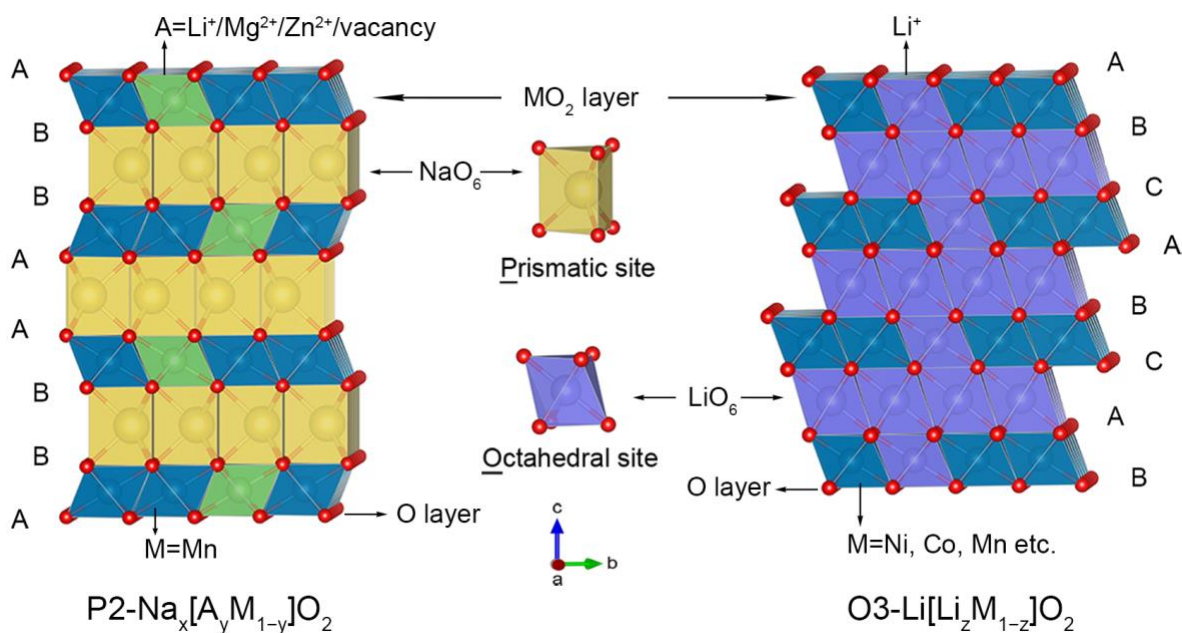
Fig. S1. Comparison of crystal structures and chemical compositions between Na-deficient oxygen-redox layered oxides and Li-rich layered oxides. In general, the labels P and O indicate that alkali metal ions are respectively located in the prismatic sites and octahedral sites, and the figures represent the number of oxide layer packings in a single unit cell (2: ABBA; 3: ABCABC).[8] The transition metal ion migration from MO_2 layers to alkali metal layers is difficult to achieve in the Na-deficient layered oxides.[9]
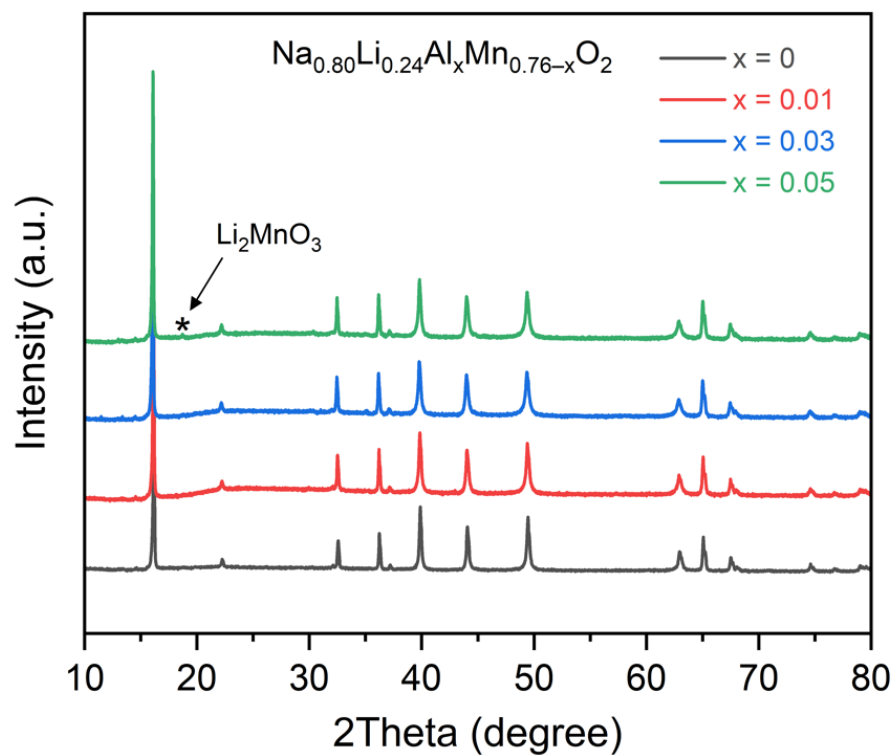
Fig. S2. XRD patterns of Na$_{0.8}$Li$_{0.24}$Al$_x$Mn$_{0.76-x}$O$_2$ (x = 0, 0.01, 0.03, 0.05). The excess of Al substitution content leads to the formation of Li$_2$MnO$_3$ phase for Na$_{0.8}$Li$_{0.24}$Al$_{0.05}$Mn$_{0.71}$O$_2$.
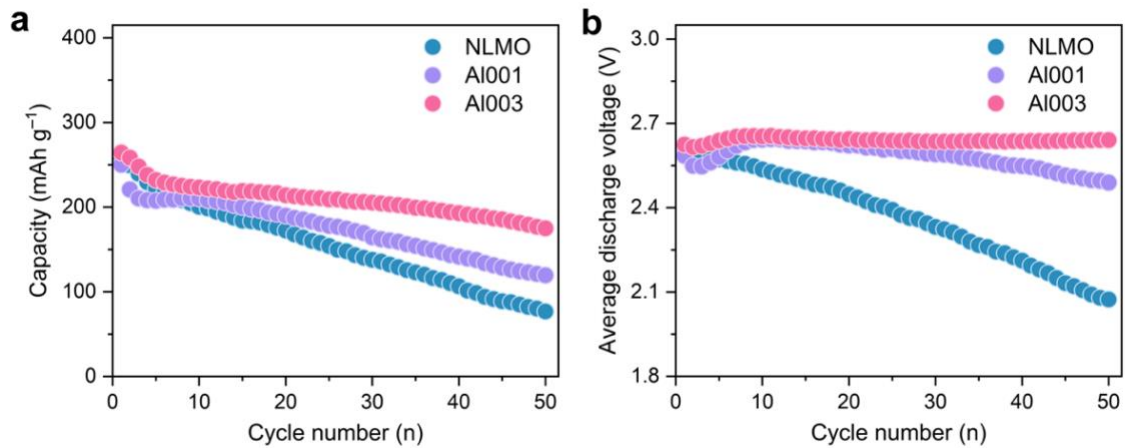
**Fig. S3.** (a,b) Comparison of discharge capacity (a) and average discharge voltage (b) for Na$_{0.8}$Li$_{0.24}$Al$_x$Mn$_{0.76-x}$O$_2$ (x = 0, 0.01, 0.03).
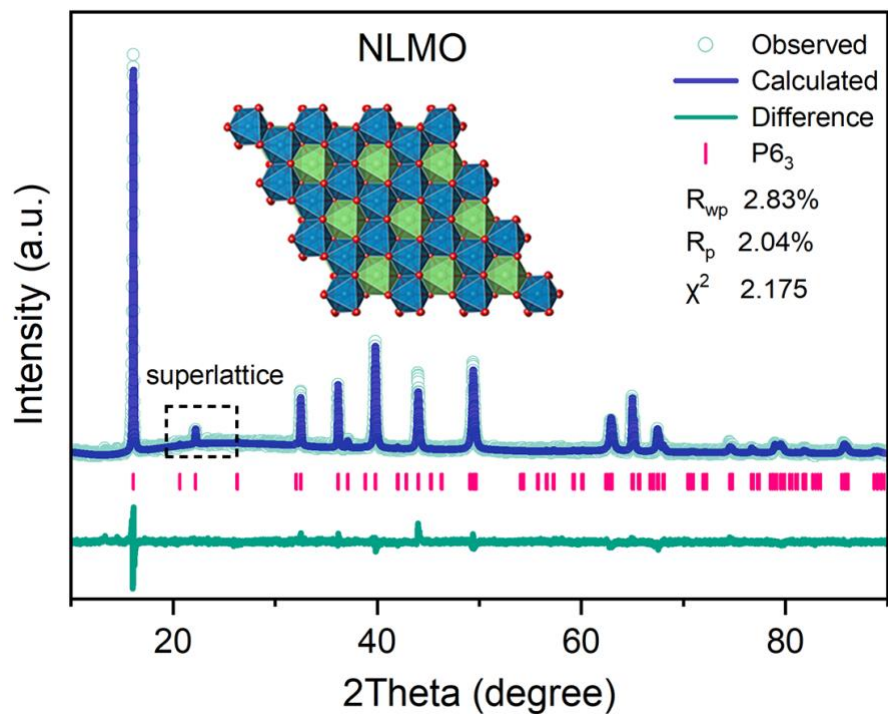
Fig. S4. Rietveld refined XRD pattern of $Na_{0.8}Li_{0.24}Mn_{0.76}O_2$ in P6$_3$ space group. All the diffraction peaks can be well indexed to a hexagonal P2-type structure with the P6$_3$ space group. The weak diffraction peak at ~22° can be matched with the Li/Mn in-plane honeycomb ordering within the MO$_2$ layers, as illustrated in the inset.[10]
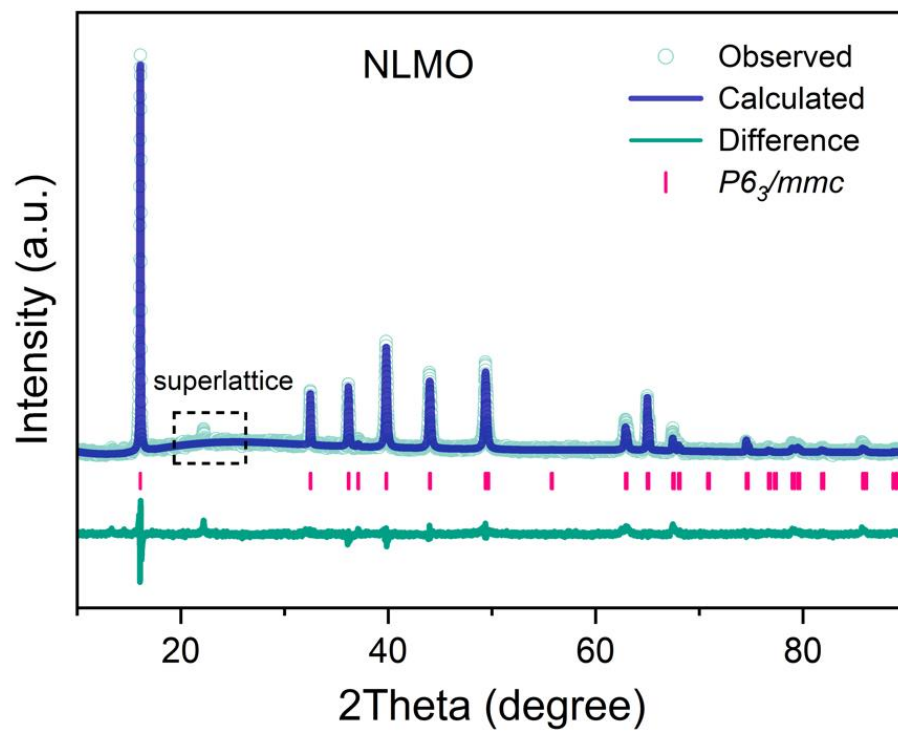
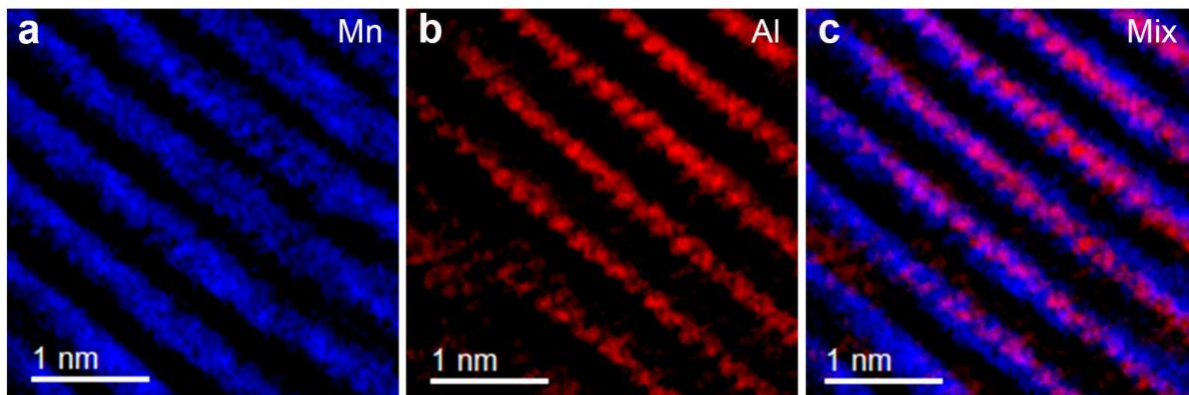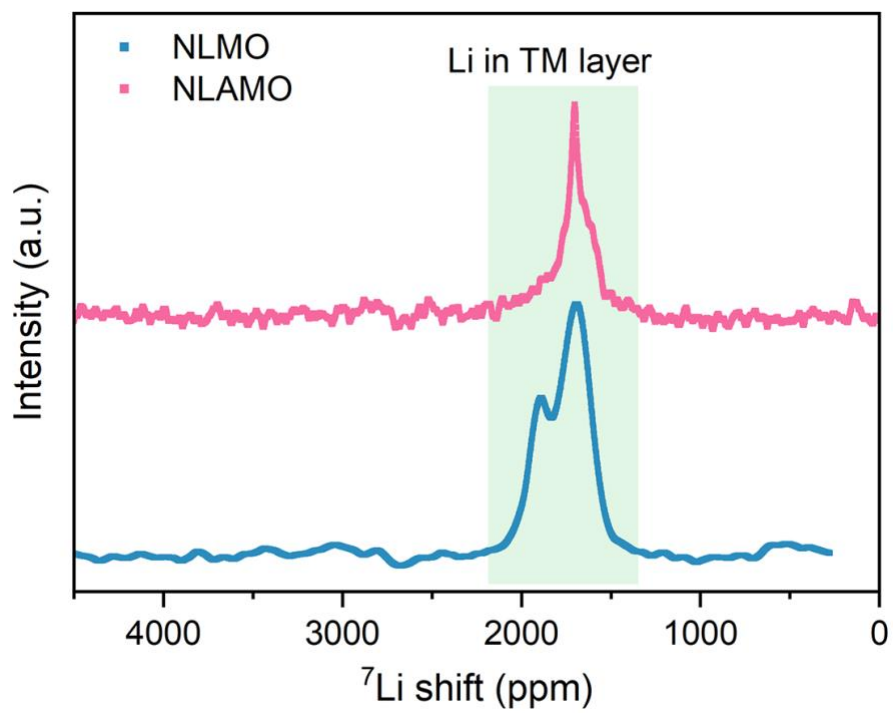**Fig. S5.** Rietveld refined XRD pattern of $Na_{0.8}Li_{0.24}Mn_{0.76}O_2$ in $P6_3/mmc$ space group.
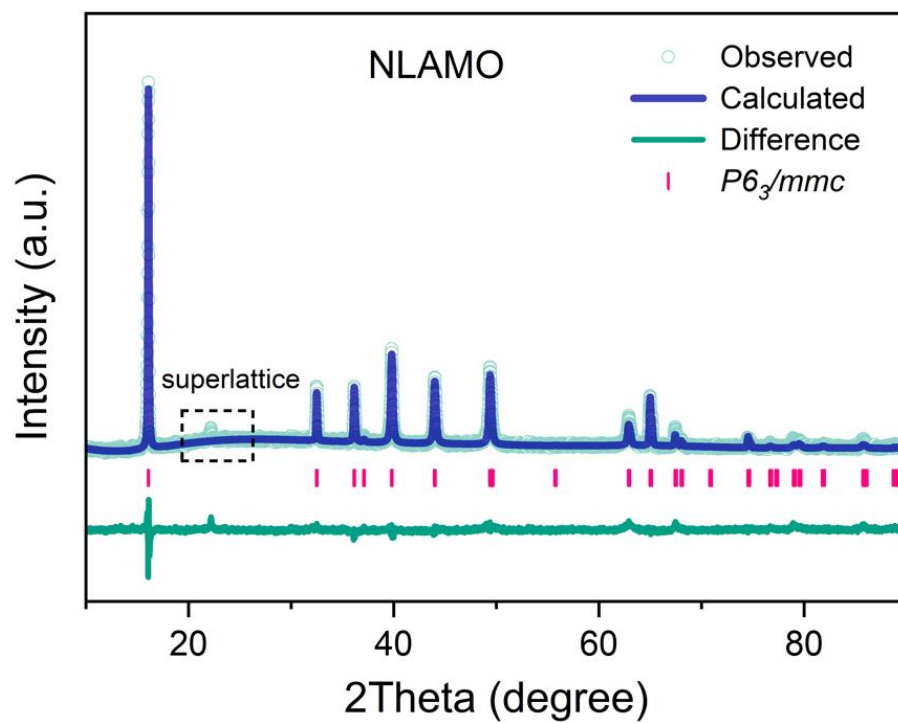
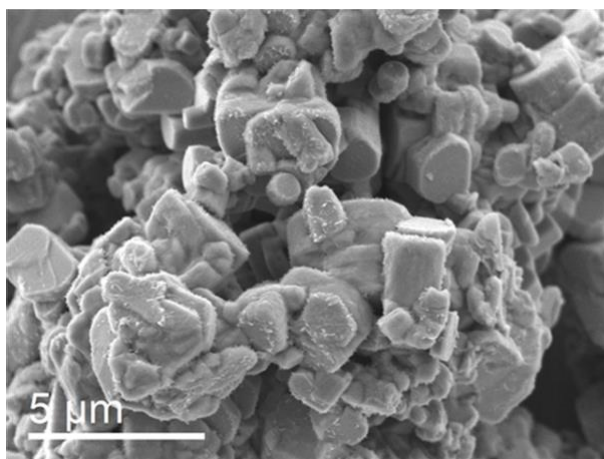**Fig. S6.** Rietveld refined XRD pattern of $Na_{0.8}Li_{0.24}Al_{0.03}Mn_{0.73}O_2$ in $P6_3/mmc$ space group.
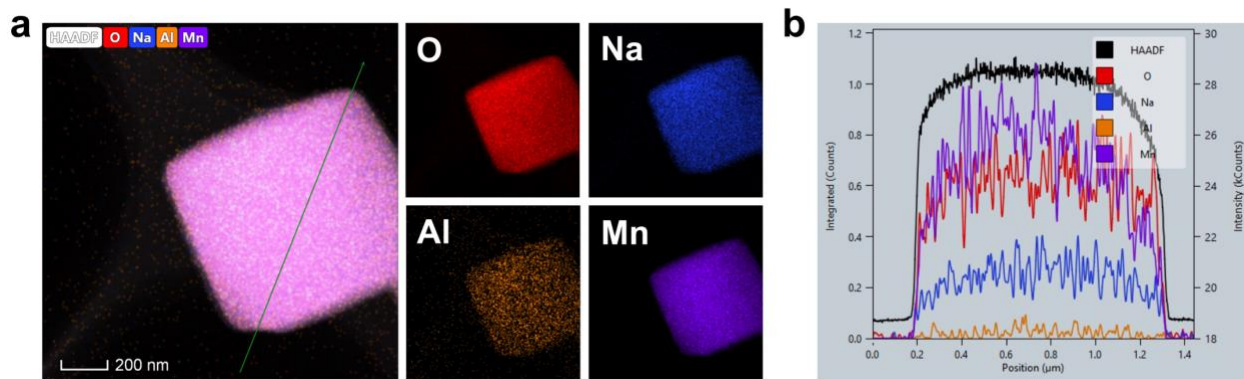
Fig. S7. EFTEM images of NLAMO. (a,,b) The compositional EFTEM maps of Mn (a) and Al (b), respectively. (c) The color-coded mixed compositional map.
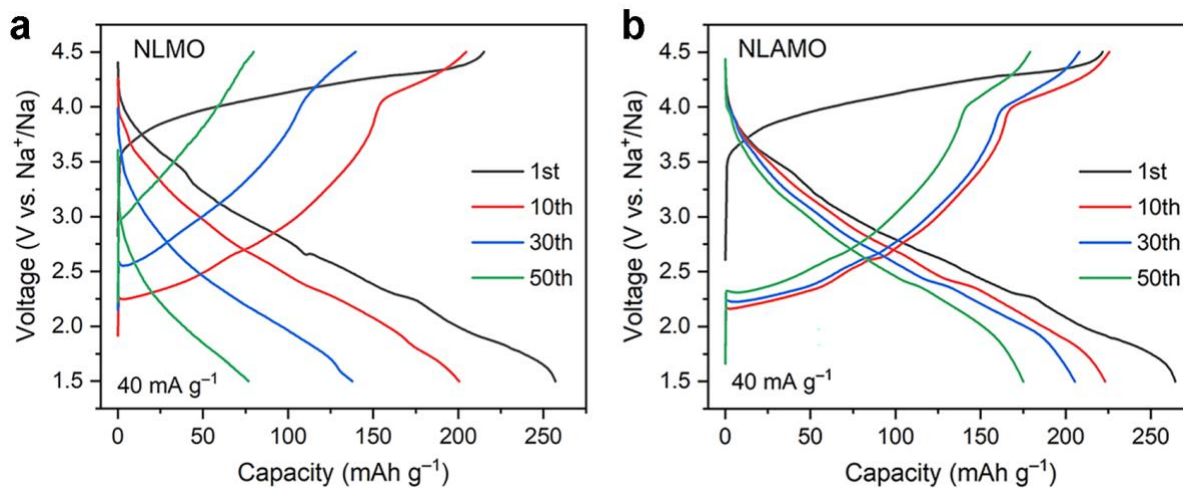
Fig. S8. Solid-state ^{7}Li NMR spectra of NLMO and NLAMO. The resonance observed at 1500–2000 ppm can be attributed to the Li ions in the MO_2 layers.[11]
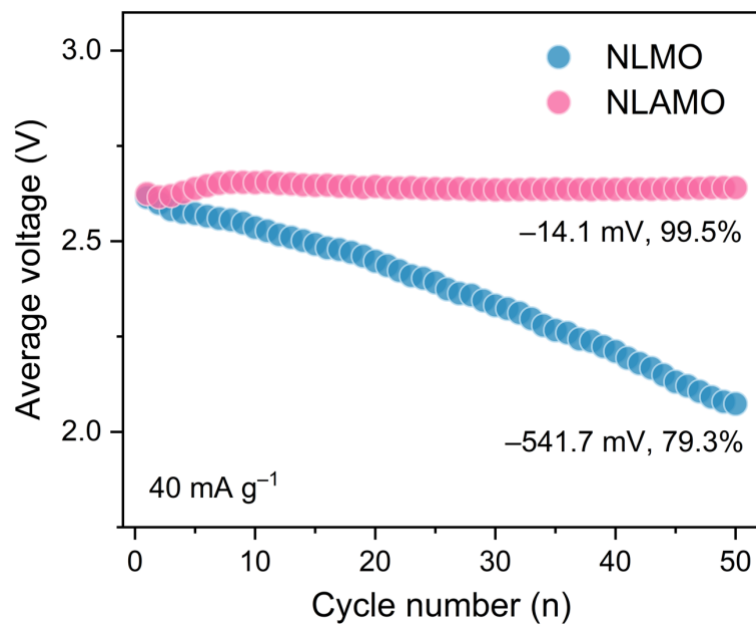
Fig. S9. SEM image of NLAMO.

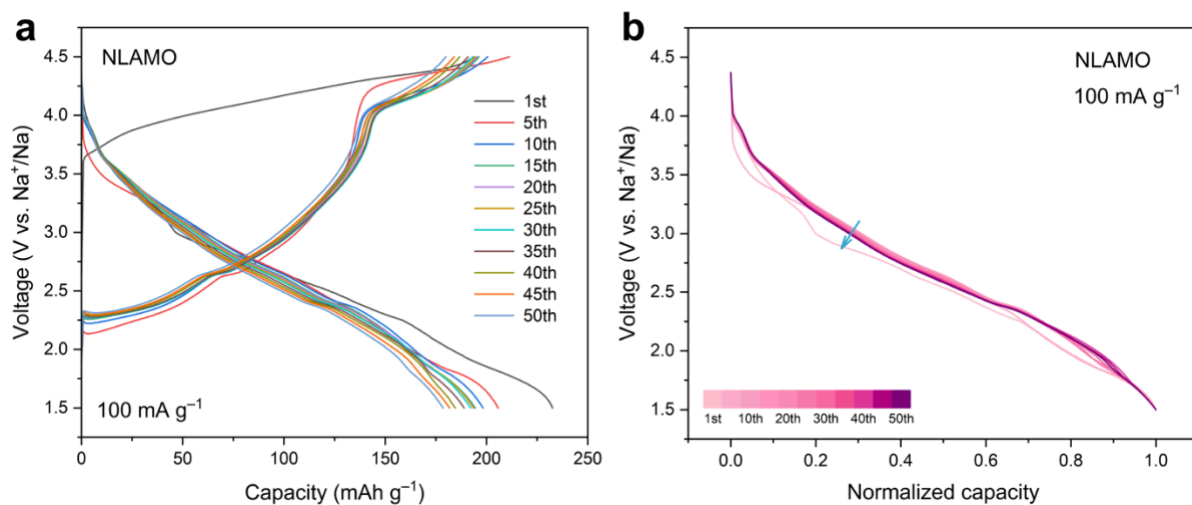**Fig. S10.** (a,b) TEM-EDS mappings (a) and line scan profiles (b) of NLAMO.

Fig. S11. (a,b) Galvanostatic charge-discharge profiles of NLMO (a) and NLAMO (b) at the 1st, 10th, 30th and 50th cycles within the voltage range of 1.5–4.5 V at a current density of 40 mA g^{-1} (0.2 C).
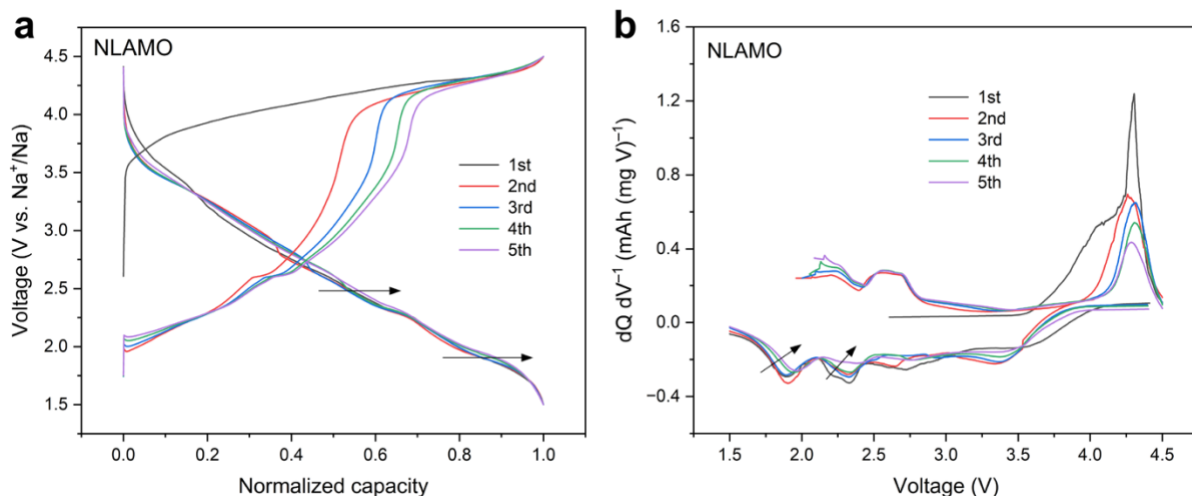
Fig. S12. Comparison of average voltage retention between NLMO and NLAMO over 50 cycles at a current density of 40 mA g^{-1}.

Fig. S13. (a,b) Galvanostatic charge-discharge profiles (a) and normalized discharge curves (b) of NLAMO at representative cycles within the voltage range of 1.5–4.5 V at a current density of 100 mA g^{-1}.

Fig. S14. (a,b) Normalized charge-discharge profiles (a) and differential capacity ($dQ\ dV^{-1}$) curves (b) of NLAMO for the early cycles within the voltage range of 1.5–4.5 V at a current density of 40 mA g^{-1}. It is observed that the Mn^{3+}/Mn^{4+} redox peaks gradually shift to higher voltage and the length of oxygen redox plateaus shortens, indicating the charge compensation mechanism evolution affected by the side reactions between electrolytes and oxygen species at high voltage, which leads to the voltage rise in the early cycles.
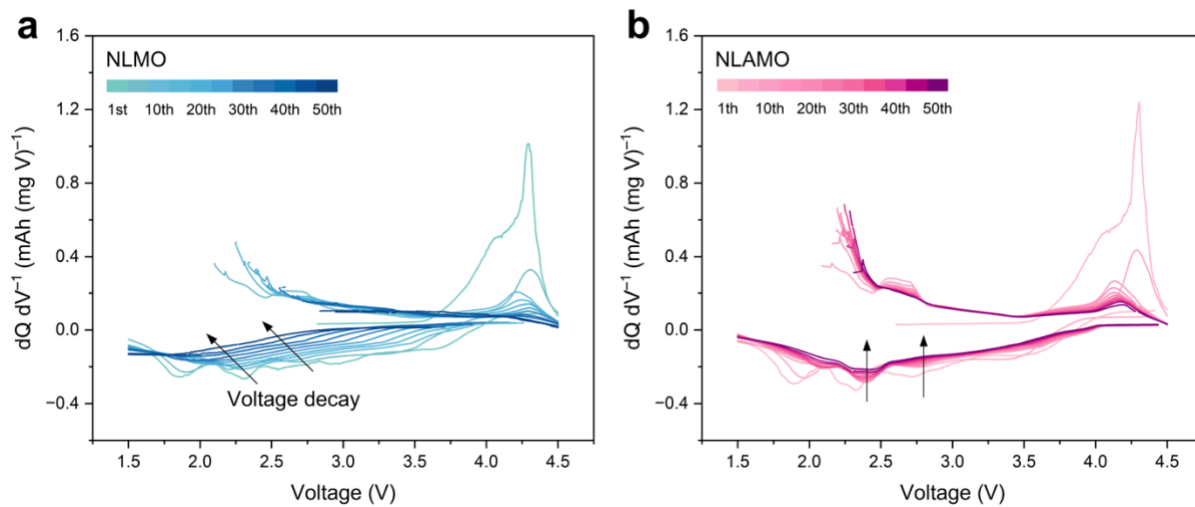
Fig. S15. (a,b) Differential capacity curves of NLMO (a) and NLAMO (b) within the voltage range of 1.5–4.5 V at a current density of 40 mA g^{-1}.
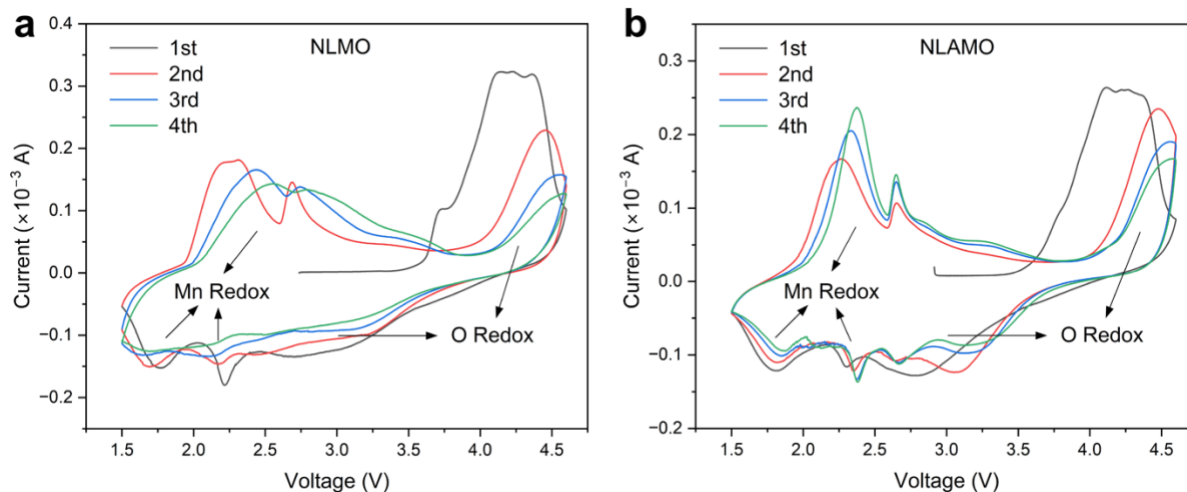
Fig. S16. (a,b) Cyclic voltammetry curves of NLMO (a) and NLAMO (b) at a scan rate of 0.2 mV s^{-1} from the 1st to 4th cycles. Low-voltage Mn redox and high-voltage O redox contribute to the charge and discharge capacity. For NLMO, both O redox and Mn redox are significantly irreversible because of O$_2$ release and the resultant steric Mn redox heterogeneity, resulting in voltage decay. Comparatively, the electrochemical stability of NLAMO is significantly enhanced with more reversible O redox and Mn redox due to the electron localization of Al.
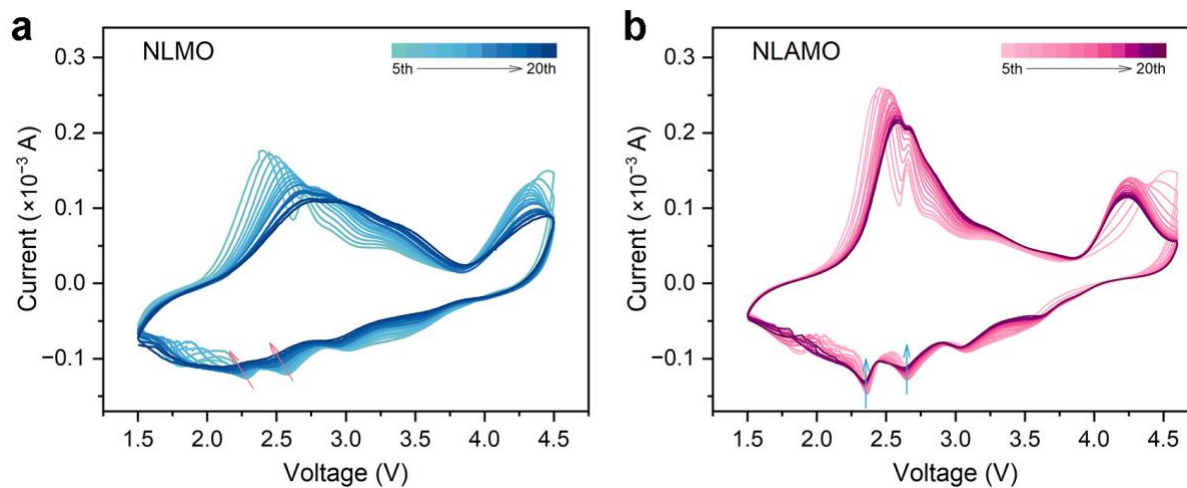
Fig. S17. (a,b) Cyclic voltammetry curves of NLMO (a) and NLAMO (b) at a scan rate of 0.2 mV s^{-1} from the 5th to 20th cycles. In the discharge process, the reduction peaks associated with manganese shift to the left upon cycling for NLMO. By contrast, this change is absent for NLAMO, which confirms the suppressed voltage decay.
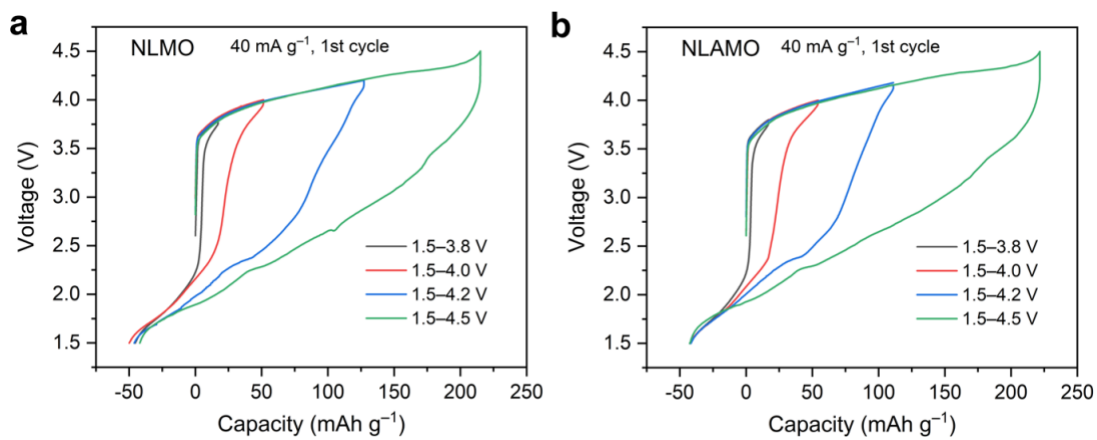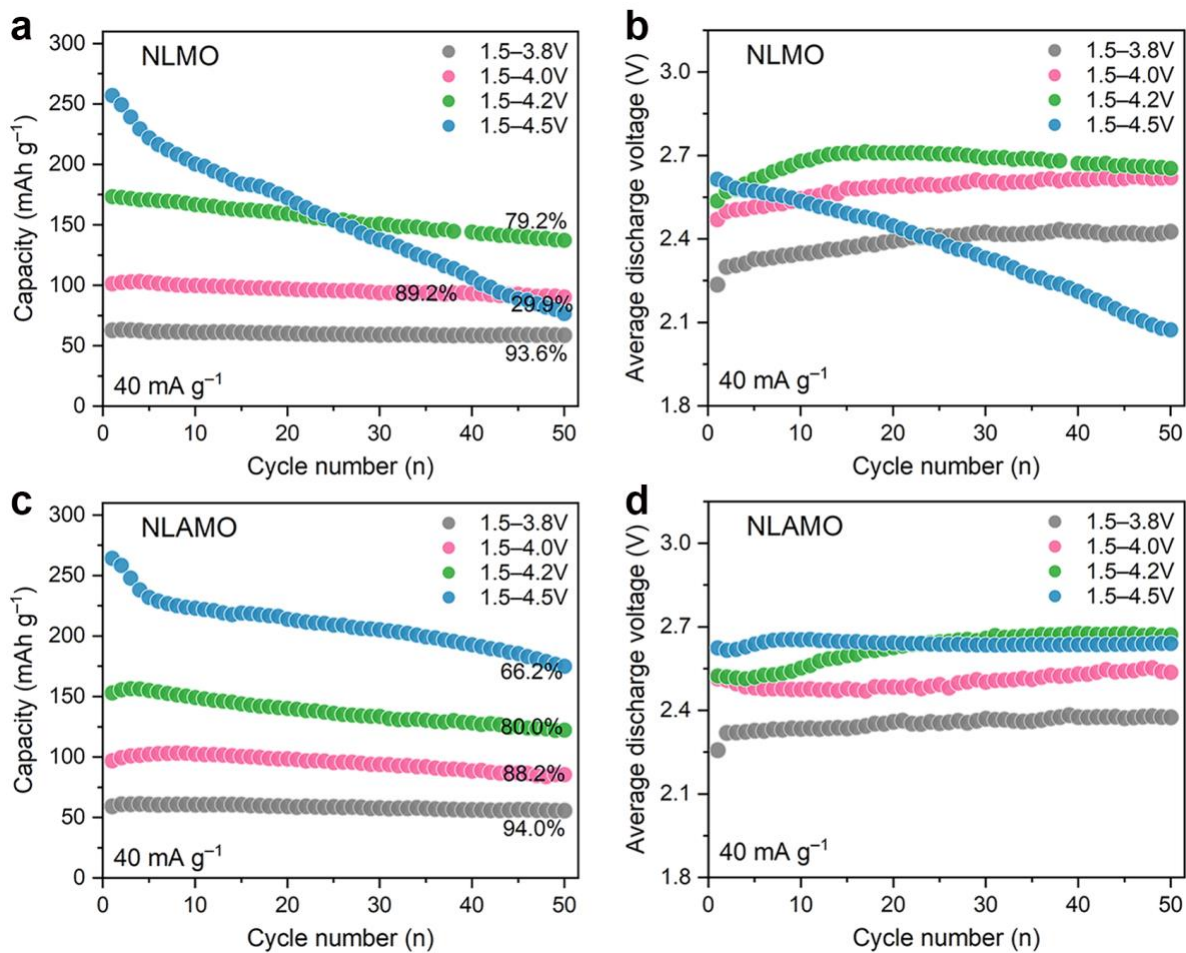
Fig. S18. (a,b) Galvanostatic charge-discharge profiles of NLMO (a) and NLAMO (b) within different voltage range at a current density of 40 mA g^{-1}.

Fig. S19. Electrochemical performance comparison within different charge voltage windows. (a,c) Capacity retention of NLMO (a) and NLAMO (c). (b,d) Average discharge voltage retention of NLMO (b) and NLAMO (d).
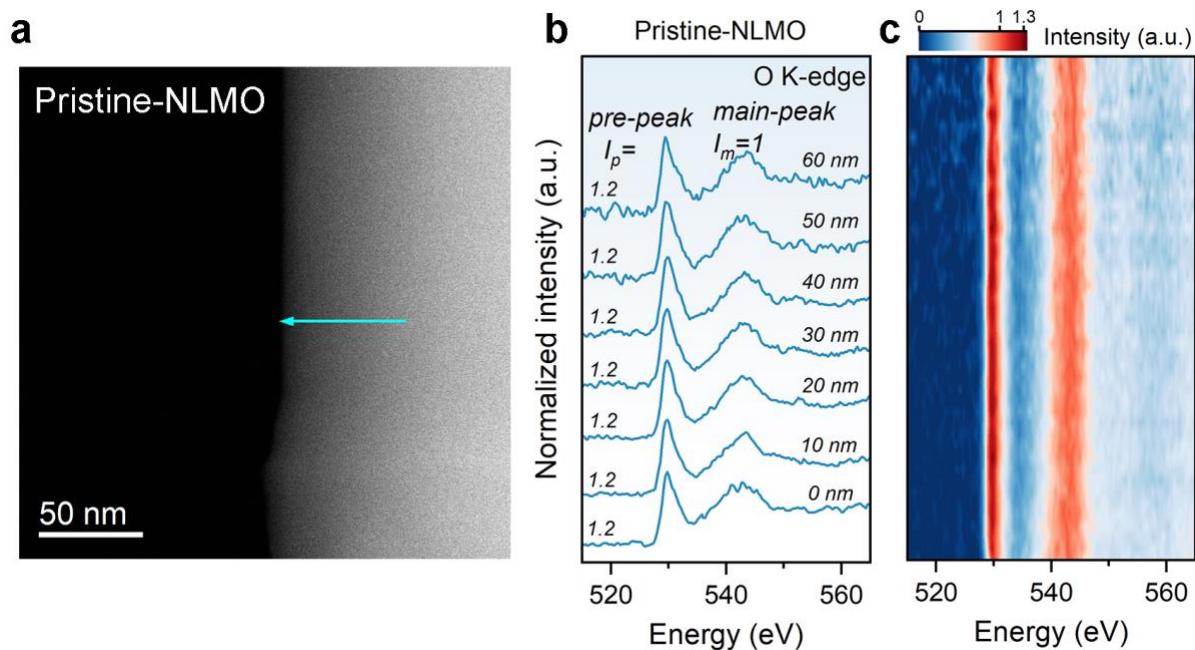
Fig. S20. Oxygen oxidation states in the pristine NLMO. (a) STEM image. The arrow illustrates the direction of the EELS line scan. (b) The O K-edge EELS spectra obtained from the line scan in (a). (c) T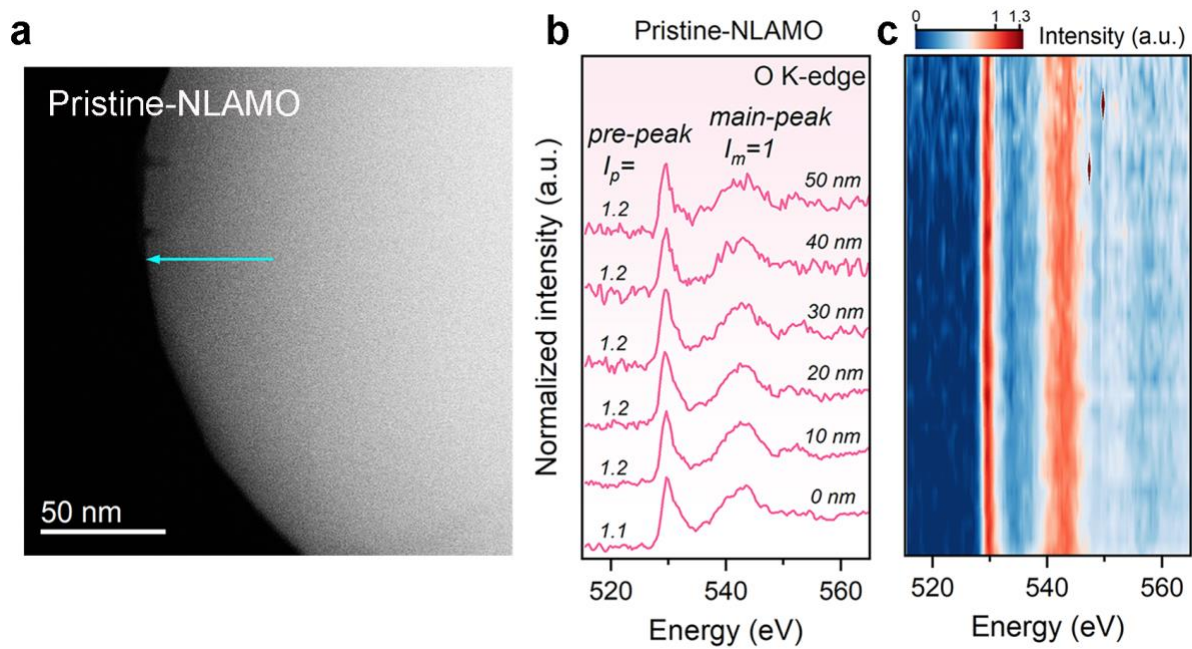he contour plot of the O K-edge EELS spectra. Each spectrum is extracted with a step interval of 1.5 nm and normalized using the main-peak signal intensity. Thus, the intensity of the main-peak (abbreviated to I_m) is 1, and the intensity of the pre-peak (abbreviated to I_p) is used to evaluate the oxygen oxidation state. The intensity of the pre-peaks is constant from the bulk to the surface.[12]
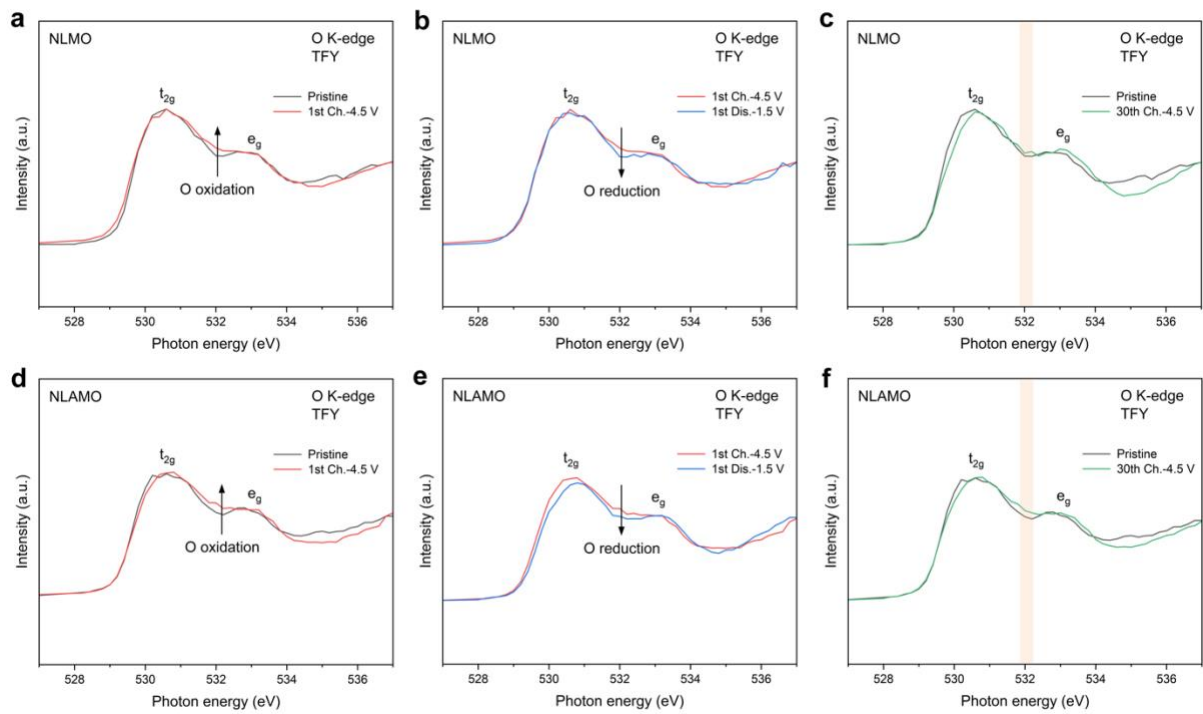
Fig. S21. Oxygen oxidation states in the pristine NLAMO. (a) STEM image. The arrow illustrates the direction of the EELS line scan. (b) The O K-edge EELS spectra obtained from the line scan in (a). (c) The contour plot of the O K-edge EELS spectra.

Fig. S22. (a–f) O K-edge Soft XAS spectra of NLMO (a–c) and NLAMO (d–f) at different states in TFY mode.
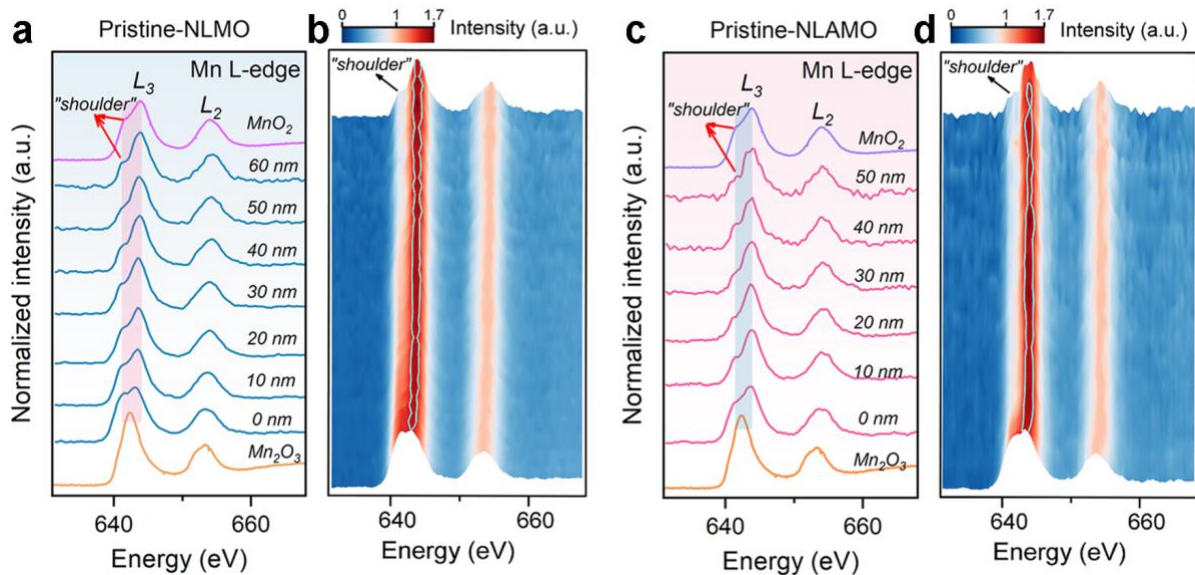
Fig. S23. Mn oxidation states in the pristine NLMO and NLAMO. (a,b) The Mn L-edge EELS spectra (a) and the contour plot (b) obtained from the line scan in Fig. S20a for NLMO. (c,d) The Mn L-edge EELS spectra (c) and the contour plot (d) obtained from the line scan in Fig. S21a for NLAMO. Each spectrum is extracted with a step interval of 1.5 nm and normalized using the L_2 signal intensity. The oxidation state of Mn can be determined by the shape of L-edge.[13]
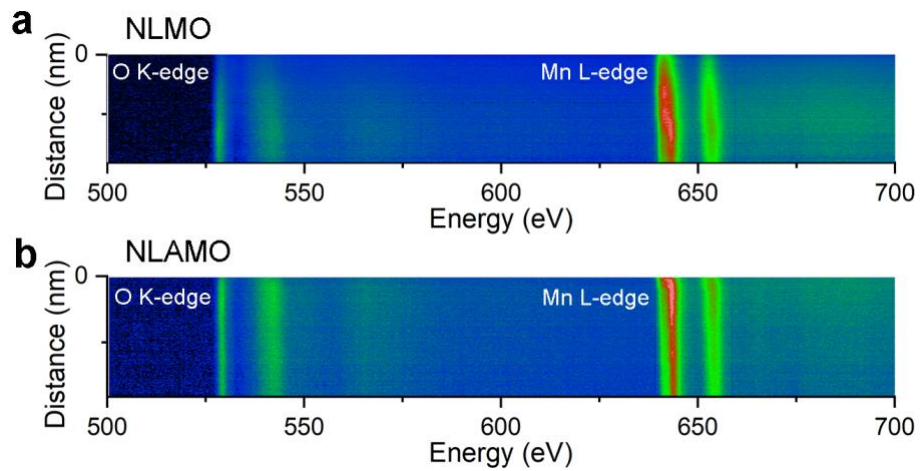
Fig. S24. (a,b) The raw EELS spectra images obtained from the line scan in Fig. 2c for NLMO (a) and from Fig. 2e for NLAMO (b).
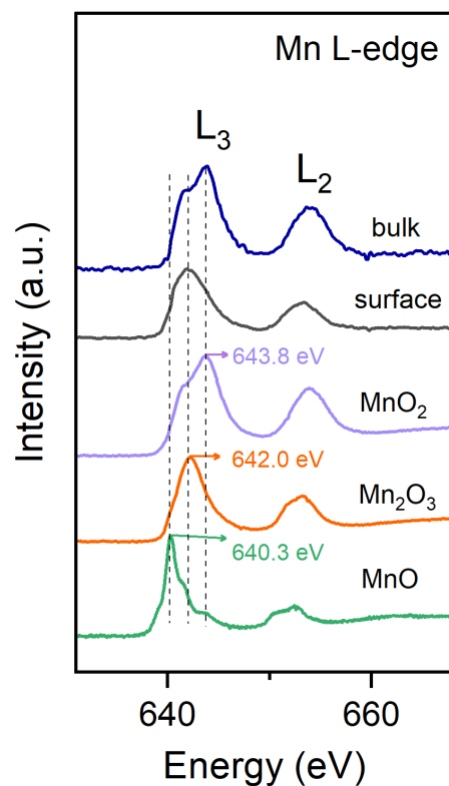
Fig. S25. The EELS spectra comparison. The blue spectrum is a representative Mn L-edge EELS spectrum obtained from the interior region in Fig. 2c, which resembles the MnO_2 reference spectrum in terms of peak position and shape. The black spectrum is extracted from the outmost surface region, which is similar to the Mn_2O_3 reference sample. The peak position of MnO reference spectrum is in a lower energy, so it is not considered in the subsequent quantitative analysis.
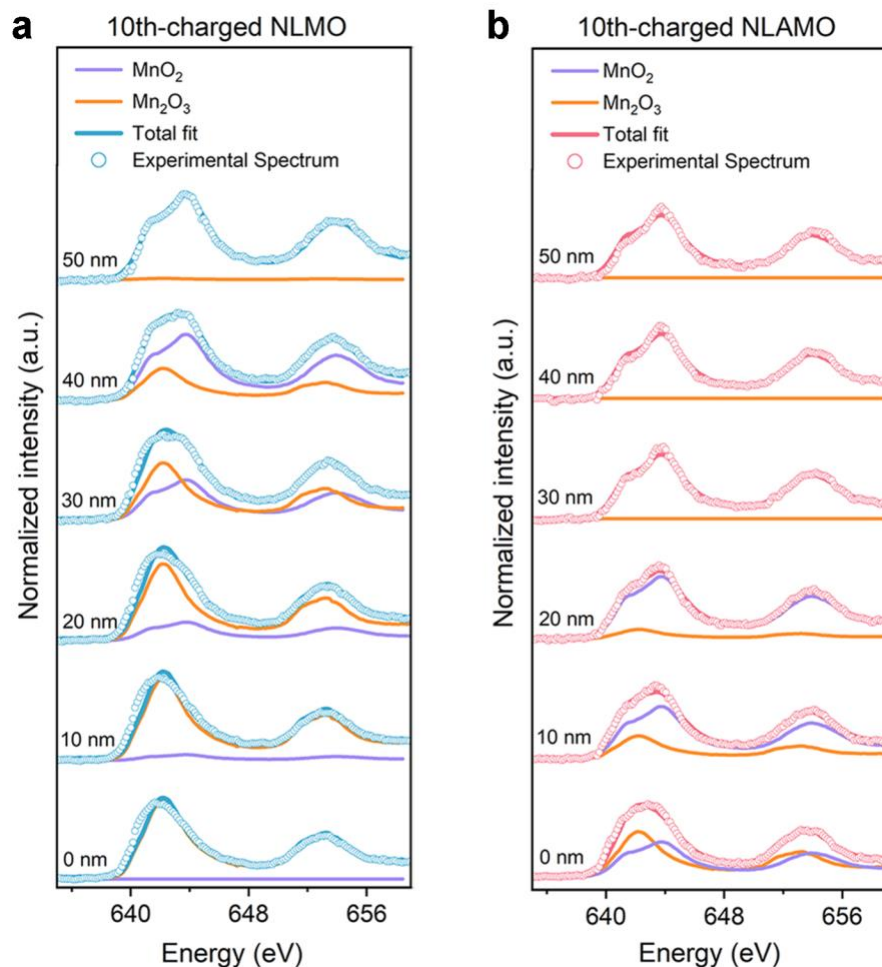
Fig. S26. Quantification of Mn oxidation states at different probing positions. (a,b) The extracted Mn L-edge EELS spectra (empty circles) and fitted spectra (solid line) for the 10th-charged NLMO (a) and NLAMO (b). A quantitative analysis based on reference samples (Mn_2O_3 and MnO_2) is performed by the multiple linear least-square (MLLS) fitting method and the results are presented in Fig. S27.
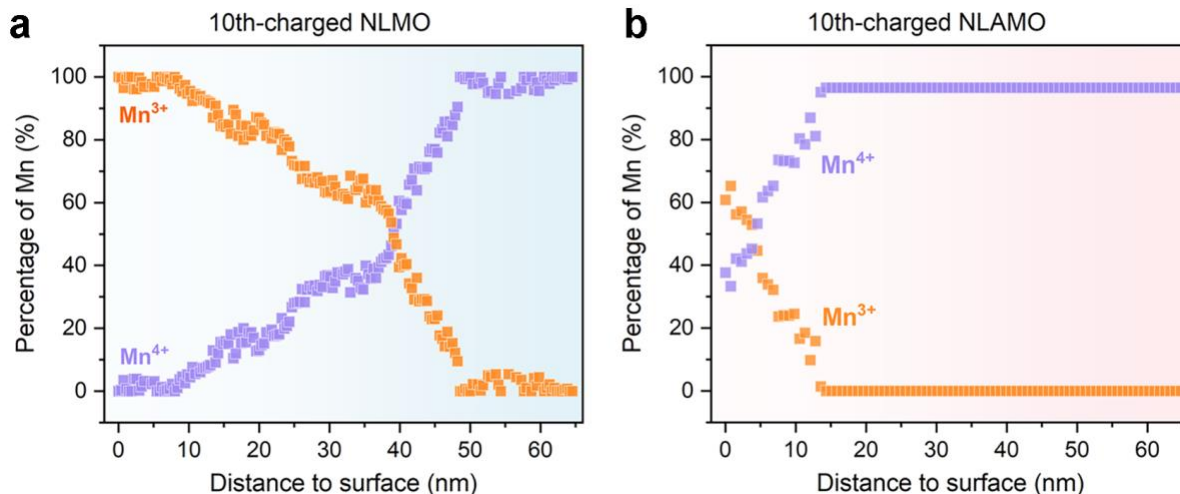
Fig. S27. (a,b) Quantitative results of Mn oxidation state for the 10th-charged NLMO (a) and NLAMO (b). In case of the 10th-charged NLMO, the content of Mn^{3+} decreases while the content of Mn^{4+} increases from surface to bulk, exhibiting a gradient distribution in the oxidation state of the Mn ions. By contrast, besides a handful of Mn^{3+} at the surface, there is a uniform Mn^{4+} distribution in the 10th-charged NLAMO.
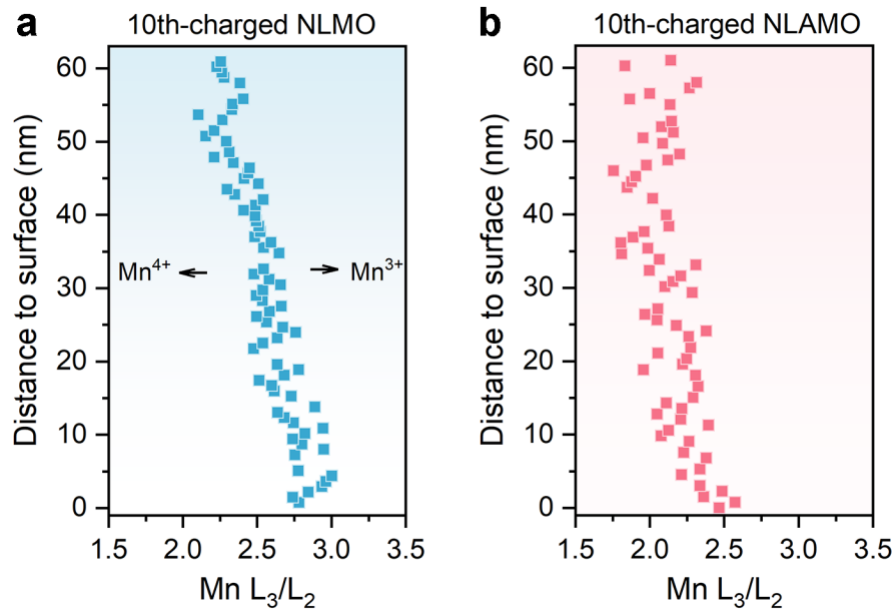
Fig. S28. (a,b) Bulk-to-surface variations in the Mn L-edge of the 10th-charged NLMO (a) and NLAMO (b). L_3/L_2 intensity ratios are sensitive to the oxidation state of Mn.[14] The results are consistent with the conclusions obtained from MLLS fitting method.
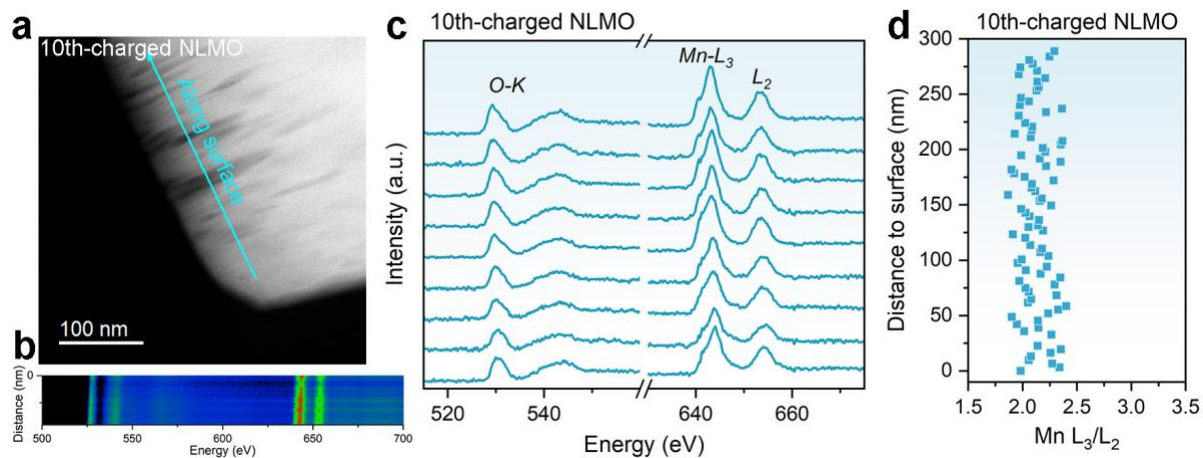
Fig. S29. The EELS spectra along surface in the 10th-charged NLMO. (a) STEM image. The arrow illustrates the direction of the EELS line scan. (b) The raw EELS spectra image obtained from the line scan in (a). (c) The extracted EELS spectra of O K-edges and Mn L-edges. (d) L_3/L_2 intensity ratios.
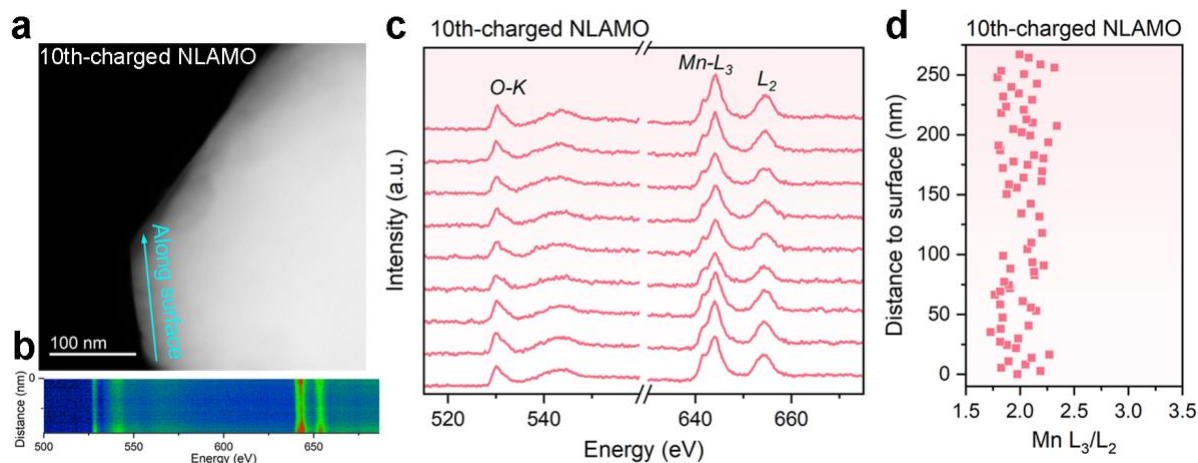
Fig. S30. The EELS spectra along surface in the 10th-charged NLAMO. (a) STEM image. The arrow illustrates the direction of the EELS line scan. (b) The raw EELS spectra image obtained from the line scan in (a). (c) The extracted EELS spectra of O K-edges and Mn L-edges. (d) L_3/L_2 intensity ratios.
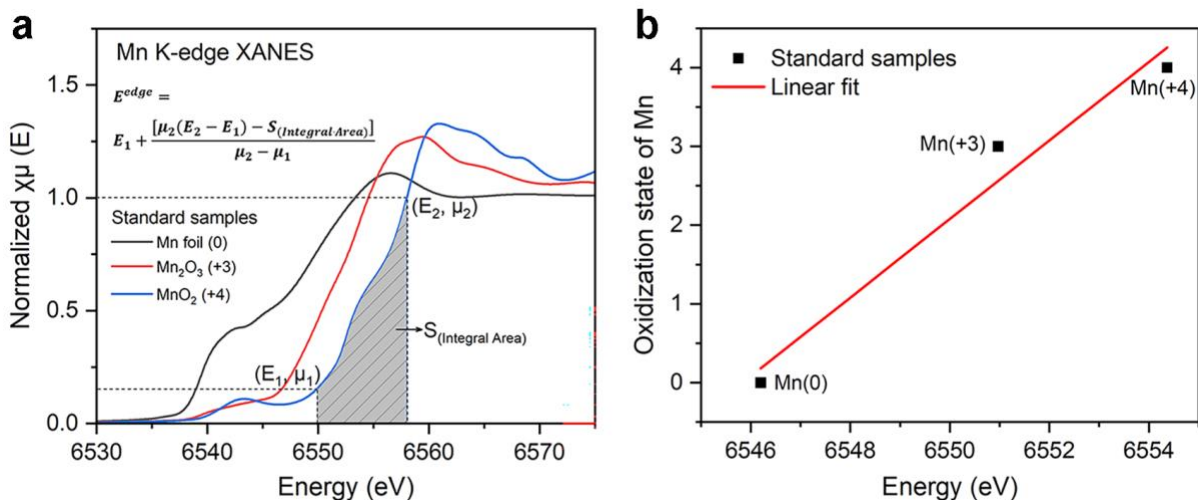
Fig. S31. (a) Normalized Mn K-edge XANES spectra of Mn foil, Mn_2O_3 and MnO_2 reference samples. (b) Linear relationship between the oxidation states of Mn and the K-edge positions determined by the integral method. The average Mn oxidation states of all samples at different charged and discharged sates can be approximately deduced from this fitted line. Considering the effect of the variation in the shape of the absorption edge on the average edge energy due to the coordination environment change, the integral method is adopted and integration is performed between $\mu_1 = 0.15$ and $\mu_2 = 1.0$ on each normalized spectrum.[15, 16]
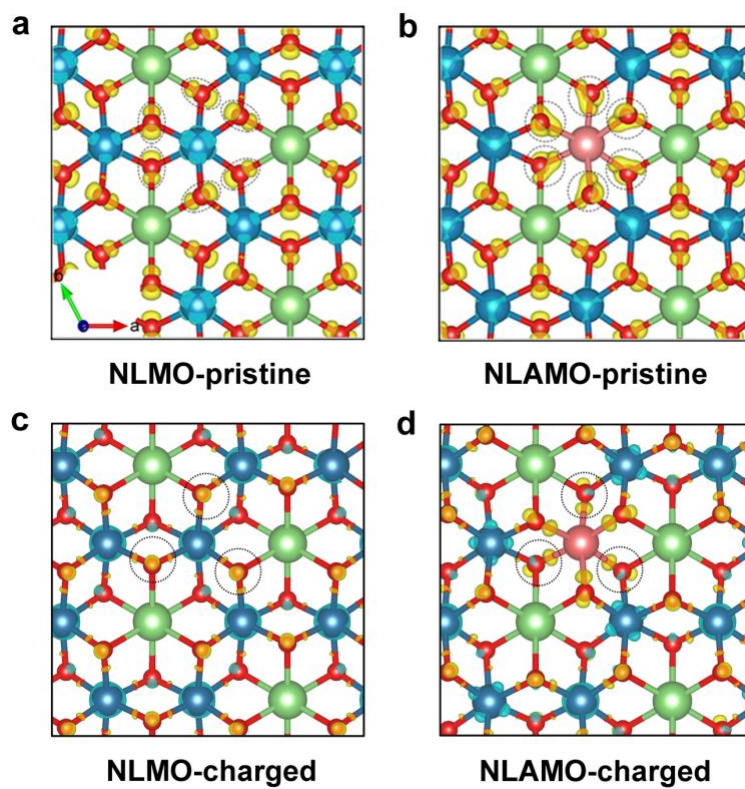
Fig. S32. (a–d) Charge density difference of the pristine NLMO (a), NLAMO (b) and the charged NLMO (c), NLAMO (d).
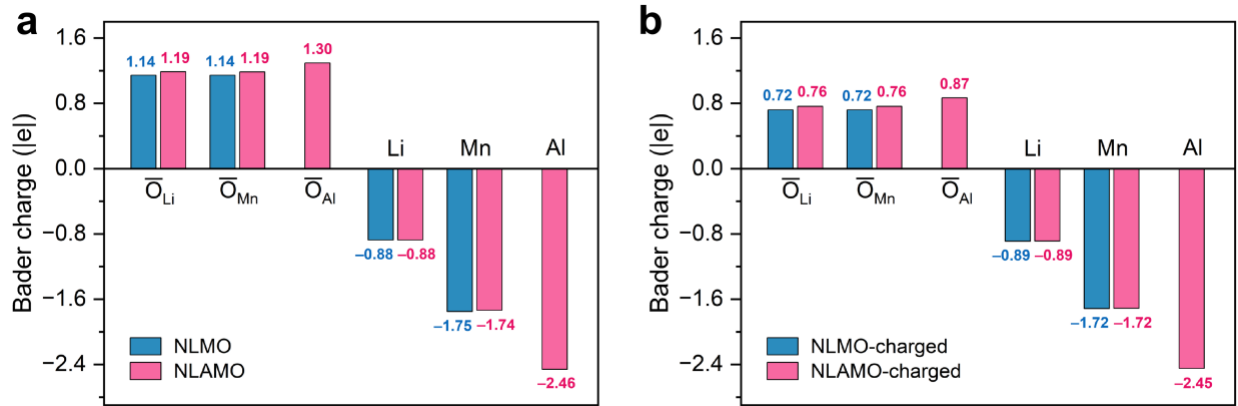
Fig. S33. (a,b) Charge transfer number of different atoms for the pristine (a) and the charged (b) NLMO and NLAMO.
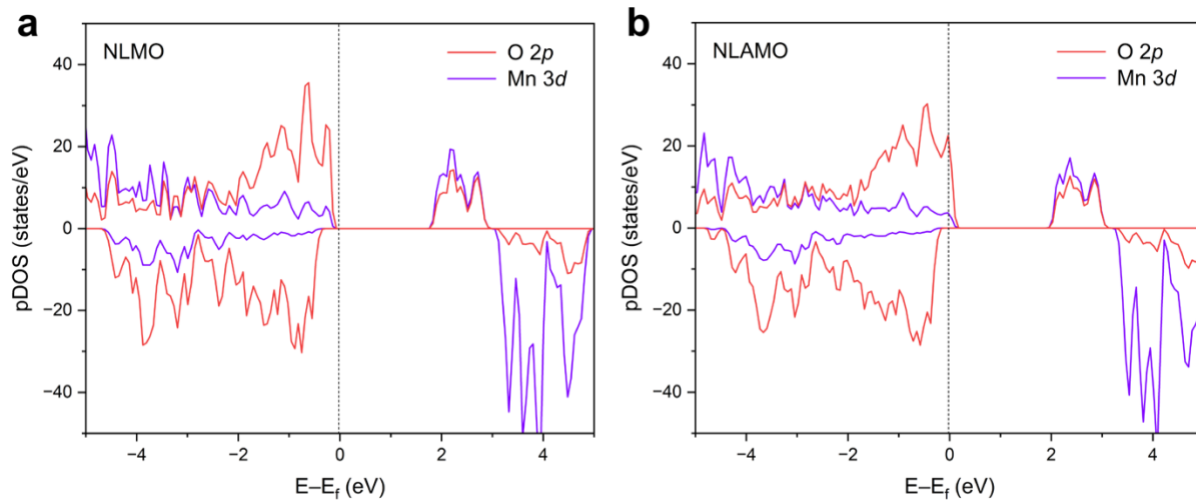
Fig. S34. (a,b) Calculated pDOS of NLMO (a) and NLAMO (b).
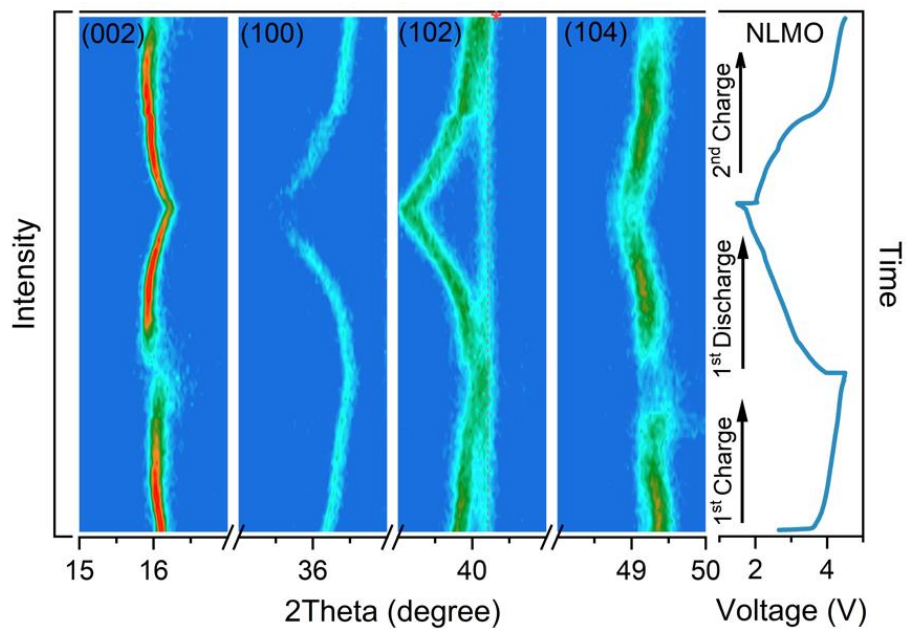
Fig. S35. The contour plot of the in-situ XRD patterns and the corresponding charge-discharge curves for NLMO.
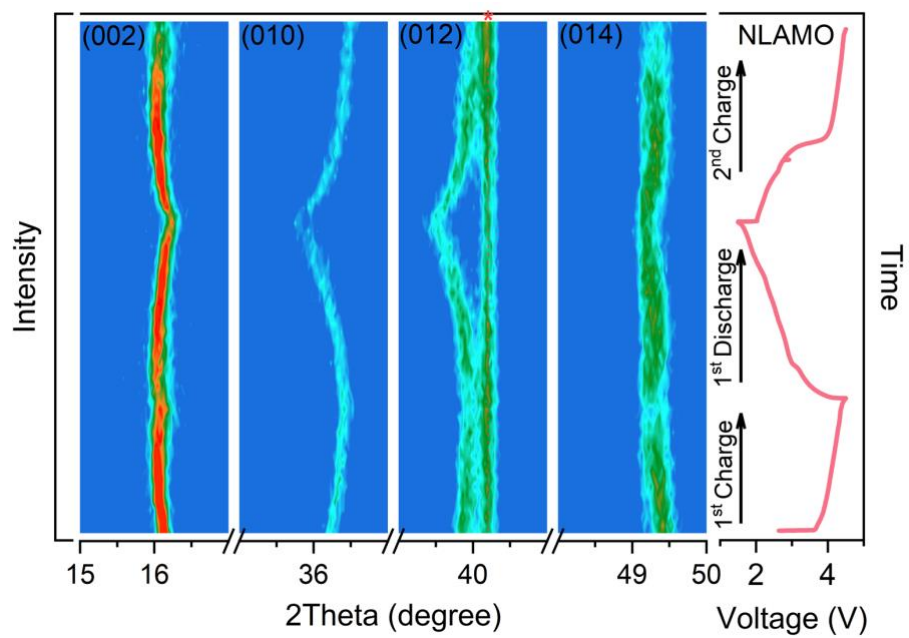
Fig. S36. The contour plot of the in-situ XRD patterns and the corresponding charge-discharge curves for NLAMO.
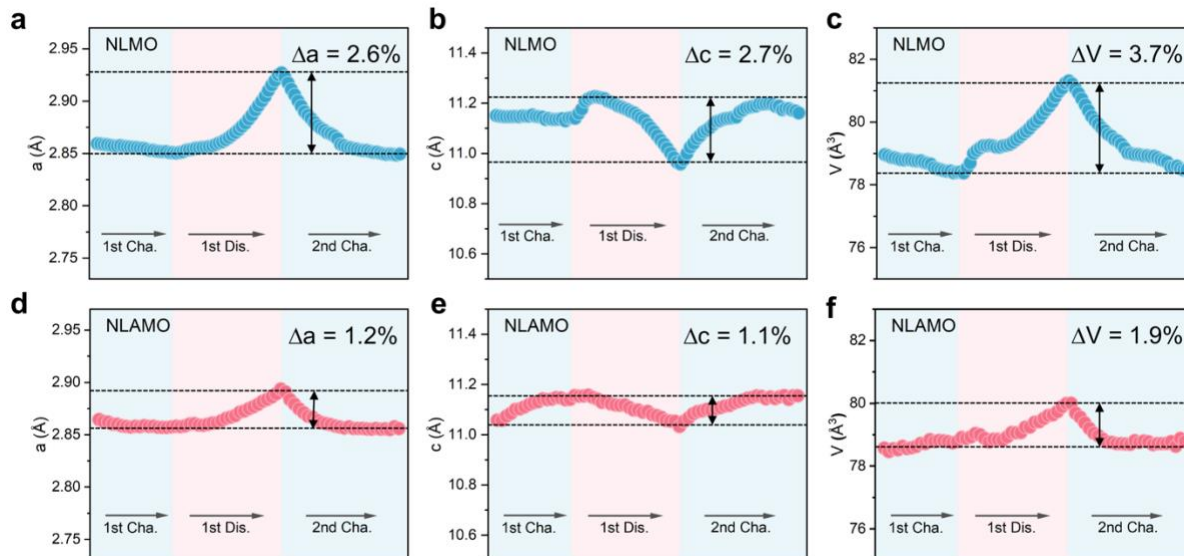
Fig. S37. (a–f) Evolution of the lattice parameters during charging and discharging for NLMO (a–c) and NLAMO (d–f).
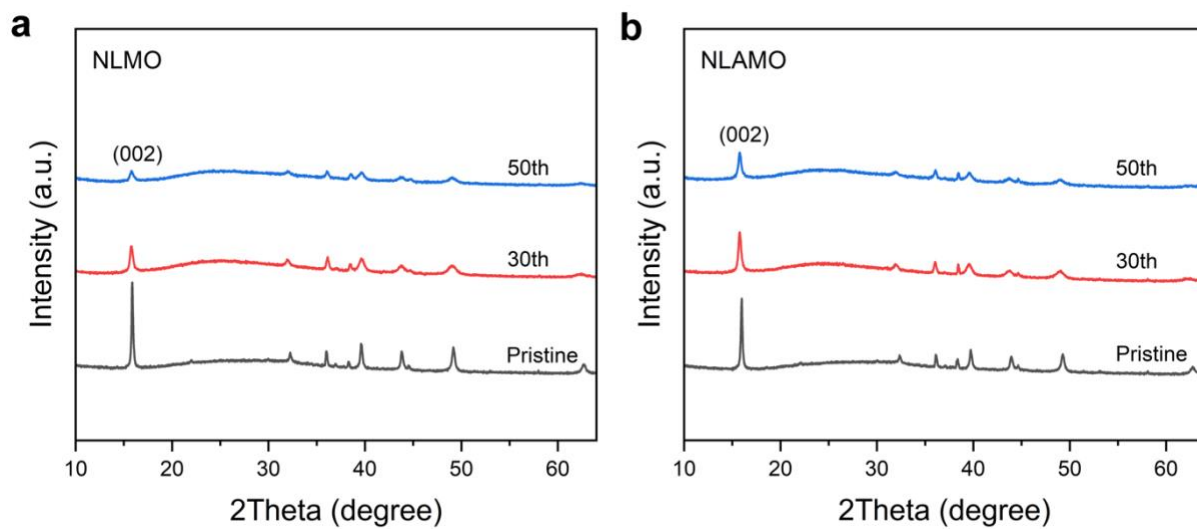
Fig. S38. (a,b) XRD patterns of NLMO (a) and NLAMO (b) at different cycles.

Supplemental Tables

Table S1. Inductively coupled plasma-optical emission spectrometry (ICP-OES) results for NLMO and NLAMO.

Samples	Measured atomic ratio by ICP-OES			
	Na	Li	Al	Mn
$Na_{0.80}Li_{0.24}Mn_{0.76}O_2$	0.7920	0.2454	0	0.7546
$Na_{0.80}Li_{0.24}Al_{0.03}Mn_{0.73}O_2$	0.8113	0.2368	0.0274	0.7358

Table S2. Detailed Rietveld refinement results of the XRD pattern for $Na_{0.80}Li_{0.24}Mn_{0.76}O_2$.

Atom	Site	x	y	z	g (Occupancy)
Na1	6c	0.730	0.397	0.250	0.089(1)
Na2	6c	0.064	0.064	0.250	0.089(1)
Na3	6c	0.397	0.730	0.250	0.089(1)
Na4	6c	0.606	0.606	0.250	0.175(1)
Na5	6c	0.728	2/3	0.250	0.175(1)
Na6	6c	2/3	0.728	0.250	0.175(1)
Li1	2b	2/3	1/3	0	0.317(4)
Mn1	2b	2/3	1/3	0	0.683(4)
Li2	2b	1/3	2/3	0	0.061(4)
Mn2	2b	1/3	2/3	0	0.939(4)
Li3	2a	0	0	0	0.358(8)
Mn3	2a	0	0	0	0.642(8)
O1	6c	0.018	0.698	0.088	1
O2	6c	0.315	0.990	0.906	1

$Na_{0.80}Li_{0.24}Mn_{0.76}O_2$, Space group: $P6_3$

$a = b = 4.96808(6)$ Å, $c = 11.02202(18)$ Å, $V = 235.596(6)$ Å^3

$R_{wp} = 2.83\%$, $R_p = 2.04\%$, $\chi^2 = 2.175$

Table S3. Detailed Rietveld refinement results of the XRD pattern for $Na_{0.80}Li_{0.24}Al_{0.03}Mn_{0.73}O_2$.

Atom	Site	x	y	z	g (Occupancy)
Na1	6c	0.730	0.397	0.250	0.091(1)
Na2	6c	0.064	0.064	0.250	0.091(1)
Na3	6c	0.397	0.730	0.250	0.091(1)
Na4	6c	0.606	0.606	0.250	0.179(1)
Na5	6c	0.728	2/3	0.250	0.179(1)
Na6	6c	2/3	0.728	0.250	0.179(1)
Li1	2b	2/3	1/3	0	0.340(1)
Mn1	2b	2/3	1/3	0	0.632(2)
Al1	2b	2/3	1/3	0	0.028(1)
Li2	2b	1/3	2/3	0	0.080(2)
Mn2	2b	1/3	2/3	0	0.895(5)
Al2	2b	1/3	2/3	0	0.024(2)
Li3	2a	0	0	0	0.290(1)
Mn3	2a	0	0	0	0.680(2)
Al3	2a	0	0	0	0.030(1)
O1	6c	0.018	0.698	0.088	1
O2	6c	0.315	0.990	0.906	1

$Na_{0.80}Li_{0.24}Al_{0.03}Mn_{0.73}O_2$, Space group: $P6_3$

$a = b = 4.96777(5)Å, c = 11.03414(13)Å, V = 235.827(4) Å^3$

$R_{wp} = 2.51\%, R_p = 1.72\%, \chi^2 = 2.613$

Table S4. Detailed Rietveld refinement results of the XRD pattern for $Na_{0.80}Li_{0.24}Mn_{0.76}O_2$.

Atom	Site	x	y	z	g (Occupancy)
Na1	2b	0.0000	0.0000	0.2500	0.29
Na2	2d	0.6667	0.3333	0.2500	0.51
Li	2a	0.0000	0.0000	0.0000	0.24
Mn	2a	0.0000	0.0000	0.0000	0.76
O	4f	0.3333	0.6667	0.0924	1.00

$Na_{0.80}Li_{0.24}Mn_{0.76}O_2$, Space group: $P6_3/mmc$

$a = b = 2.8685$ Å, $c = 11.0230$ Å, $V = 78.574$ Å^3

$R_{wp} = 3.14\%$, $R_p = 2.18\%$, $\chi^2 = 2.673$

Table S5. Detailed Rietveld refinement results of the XRD pattern for $Na_{0.80}Li_{0.24}Al_{0.03}Mn_{0.73}O_2$.

Atom	Site	x	y	z	g (Occupancy)
Na1	2b	0.0000	0.0000	0.2500	0.29
Na2	2d	0.6667	0.3333	0.2500	0.51
Li	2a	0.0000	0.0000	0.0000	0.24
Mn	2a	0.0000	0.0000	0.0000	0.73
Al	2a	0.0000	0.0000	0.0000	0.03
O	4f	0.3333	0.6667	0.0924	1.00

$Na_{0.80}Li_{0.24}Al_{0.03}Mn_{0.73}O_2$, Space group: $P6_3/mmc$

$a = b = 2.8689$ Å, $c = 11.0229$ Å, $V = 78.572$ Å^3

$R_{wp} = 3.25\%$, $R_p = 2.30\%$, $\chi^2 = 2.847$

Table S6. Comparison of discharge capacity, average discharge voltage and energy density of the representative layered cathode materials after 50 cycles at a current density of 40 mA g^{-1}.

	Component	Voltage range /V	Discharge capacity /mAh g^{-1}	Average discharge voltage/V	Energy density /Wh kg^{-1}
1	$Na_{0.80}Li_{0.24}Al_{0.03}Mn_{0.73}O_2$ (This work)	1.5−4.5	175.0	2.64	462.1
2	$Na_{0.80}Li_{0.24}Mn_{0.76}O_2$	1.5−4.5	76.7	2.07	159.1
3	$Na_{0.7}Li_{0.1}Mg_{0.15}Mn_{0.75}O_2$	1.5−4.5	159.5	2.50	398.8
4	$Na_{0.66}Li_{0.18}Fe_{0.12}Mn_{0.70}O_2$	1.5−4.5	150.2	2.68	403.1
5	$Na_{0.66}Li_{0.22}Ti_{0.15}Mn_{0.63}O_2$	1.5−4.5	138.1	2.59	357.4
6	$Na_{0.75}Li_{0.15}Ni_{0.15}Mn_{0.7}O_2$	1.5−4.5	120.7	3.02	364.5
7	$Na_{0.6}Li_{0.2}Mn_{0.8}O_2$	1.5−4.5	140.9	2.72	383.5
8	$Na_{0.67}Mg_{0.28}Mn_{0.72}O_2$	1.5−4.5	108.3	2.47	267.3
9	$Na_{0.67}Zn_{0.25}Mn_{0.75}O_2$	1.5−4.6	121.9	2.36	288.3
10	$Na_{0.67}MnO_2$	1.5−4.2	97.1	2.32	225.1
11	$Na_{0.67}Fe_{0.50}Mn_{0.50}O_2$	1.5−4.3	105.3	2.40	252.7
12	$Na_{0.67}Ni_{0.33}Mn_{0.67}O_2$	1.5−4.2	113.0	2.75	310.6

Table S7. Inductively coupled plasma-optical emission spectrometry (ICP-OES) results for NLMO and NLAMO after 50 cycles.

Cathodes	Measured atomic ratio by ICP-OES			
	Na	Li	Al	Mn
$Na_{0.80}Li_{0.24}Mn_{0.76}O_2$	0.7087	0.2160	0	0.7840
$Na_{0.80}Li_{0.24}Al_{0.03}Mn_{0.73}O_2$	0.7608	0.2150	0.0333	0.7517

Supplemental References

1. B. H. Toby, *J. Appl. Crystallogr.,* 2001, **34**, 210–213.

2. B. Ravel and M. Newville, *J. Synchrotron Radiat.,* 2005, **12**, 537–541.

3. G. Kresse and J. Furthmüller, *Phys. Rev. B,* 1996, **54**, 11169.

4. J. P. Perdew, K. Burke and M. Ernzerhof, *Phys. Rev. Lett.,* 1996, **77**, 3865.

5. G. Kresse and D. Joubert, *Phys. Rev. B,* 1999, **59**, 1758.

6. A. Jain, G. Hautier, S. P. Ong, C. J. Moore, C. C. Fischer, K. A. Persson and G. Ceder, *Phys. Rev. B,* 2011, **84**, 045115.

7. C. Zhang, B. Wei, M. Wang, D. Zhang, T. Uchiyama, C. Liang, L. Chen, Y. Uchimoto, R. Zhang, P. Wang and W. Wei, *Energy Stor. Mater.,* 2022, **46**, 512–522.

8. N. Yabuuchi, K. Kubota, M. Dahbi and S. Komaba, *Chem. Rev.,* 2014, **114**, 11636–11682.

9. Q. Wang, S. Mariyappan, G. Rousse, A. V. Morozov, B. Porcheron, R. Dedryvère, J. Wu, W. Yang, L. Zhang, M. Chakir, M. Avdeev, M. Deschamps, Y.-S. Yu, J. Cabana, M.-L. Doublet, A. M. Abakumov and J.-M. Tarascon, *Nat. Mater.,* 2021, **20**, 353–361.

10. N. Yabuuchi, R. Hara, M. Kajiyama, K. Kubota, T. Ishigaki, A. Hoshikawa and S. Komaba, *Adv. Energy Mater.,* 2014, **4**, 1301453.

11. C. Li, C. Zhao, B. Hu, W. Tong, M. Shen and B. Hu, *Chem. Mater.,* 2020, **32**, 1054–1063.

12. T. Zhou, H. Wang, Y. Wang, P. Jiao, Z. Hao, K. Zhang, J. Xu, J.-B. Liu, Y.-S. He, Y.-X. Zhang, L. Chen, L. Li, W. Zhang, Z.-F. Ma, and J. Chen, *Chem,* 2022, **8**, 2817–2830.

13. S. Hwang, S. M. Kim, S.-M. Bak, S. Y. Kim, B.-W. Cho, K. Y. Chung, J. Y. Lee, E. A. Stach and W. Chang, *Chem. Mater.,* 2015, **27**, 3927–3935.

14. C. Ma, J. Alvarado, J. Xu, R. J. Clément, M. Kodur, W. Tong, C. P. Grey and Y. S. Meng, *J.

Am. Chem. Soc., 2017, **139**, 4835–4845.

15. H. Dau, P. Liebisch and M. Haumann, *Anal. Bioanal. Chem.,* 2003, **376**, 562–583.

16. X. Cao, H. Li, Y. Qiao, P. He, Y. Qian, X. Yue, M. Jia, J. Cabana and H. Zhou, *Joule,* 2022, **6**, 1290–1303.